

Striated 2D Lattice with Sub-nm 1D Etch Channels by Controlled Thermally Induced Phase Transformations of PdSe₂

Gyeong Hee Ryu, Taishan Zhu, Jun Chen, Sapna Sinha, Viktoryia Shautsova, Jeffrey C. Grossman, and Jamie H. Warner*

2D crystals are typically uniform and periodic in-plane with stacked sheet-like structure in the out-of-plane direction. Breaking the in-plane 2D symmetry by creating unique lattice structures offers anisotropic electronic and optical responses that have potential in nanoelectronics. However, creating nanoscale-modulated anisotropic 2D lattices is challenging and is mostly done using top-down lithographic methods with ≈ 10 nm resolution. A phase transformation mechanism for creating 2D striated lattice systems is revealed, where controlled thermal annealing induces Se loss in few-layered PdSe₂ and leads to 1D sub-nm etched channels in Pd₂Se₃ bilayers. These striated 2D crystals cannot be described by a typical unit cells of 1–2 Å for crystals, but rather long range nanoscale periodicity in each three directions. The 1D channels give rise to localized conduction states, which have no bulk layered counterpart or monolayer form. These results show how the known family of 2D crystals can be extended beyond those that exist as bulk layered van der Waals crystals by exploiting phase transformations by elemental depletion in binary systems.

Phase change occurs in binary element materials when the stoichiometry is modified and in bulk materials this leads to crystal structure change, described by the unit cell change.^[1–3] This material transformation process is well understood in bulk materials,^[4] but not so in ultrathin 2D layered systems. In bulk thin films, description of the phase change generally involves the central crystalline regions with little known about the buried interfaces and surface structure.^[5–7] In binary monolayer 2D crystals, excessive elemental depletion generally leads to holes or voids 2D shape (circles, hexagons, or triangles)^[8–15] and represents the lattice directions of minimum energy for

atomic removal. In the case of few layered 2D materials, void formation and surface restructuring represent a significant portion of the total structure.


Phase transitions of transition metal dichalcogenides (TMDs) have been extensively investigated.^[16–20] Among them, palladium diselenide (PdSe₂) is attracting attention due to its interesting electronic properties and atomic structure.^[21] Importantly, the layer binding energy of PdSe₂ is 190 meV per atom,^[21] which is relatively higher than graphite (≈ 35 meV per atom),^[22] h-BN (52 meV per atom),^[23] and black phosphorous (40 meV per atom)^[23] but few studies are reported about obtaining monolayer PdSe₂ by mechanical exfoliation.^[24,25] In contrast to the frequently reported hexagonal phases in TMDs, PdSe₂ has a unique structure, **Figure 1a**.^[21,23,26] In the few layered structure, Se vacancies break

the symmetry and induce large structural distortion and as a result PdSe₂ adopts pentagonal rings with the vertices in a slightly asymmetrical puckered structure that is different from other TMDs.^[27,28] Recent results showed that bilayer PdSe₂ can undergo local phase transitions into monolayer Pd₂Se₃ due to electron beam-induced Se vacancies and merging the Pd backbones from the two layers into one, which is called as an “interlayer fusion,” with a different crystal structure (**Figure 1b**).^[24] The ability of PdSe₂ to undergo crystal structure transformations opens up many opportunities for creating new 2D lattice structures that are not available as bulk van der Waals layered materials by control of Se deficiencies. Additionally, the atomic dynamics of structural defects such as bond rotations, edge termination, and grain boundaries on monolayer Pd₂Se₃ that come from PdSe₂ were reported using annular dark field-scanning transmission electron microscopy (ADF-STEM) imaging.^[27]

Here, we introduce chalcogen vacancies in PdSe₂ few layered films using in situ controlled thermal annealing in vacuum near the melting point, which is compatible with large-scale processing. The anisotropic structure and low melting point (≈ 500 °C) of PdSe₂, compared to MoS₂ (≈ 1000 °C) makes it a suitable candidate for exploring changes in structure by Se loss. The novel atomic structure is imaged using ADF-STEM and

Dr. G. H. Ryu, J. Chen, S. Sinha, Dr. V. Shautsova, Prof. J. H. Warner
Department of Materials
University of Oxford
16 Parks Road, Oxford OX1 3PH, UK
E-mail: Jamie.warner@materials.ox.ac.uk

Dr. T. Zhu, Prof. J. C. Grossman
Department of Materials Science and Engineering
Massachusetts Institute of Technology
77 Massachusetts Avenue, Cambridge, MA 02139, USA

 The ORCID identification number(s) for the author(s) of this article can be found under <https://doi.org/10.1002/adma.201904251>.

DOI: 10.1002/adma.201904251

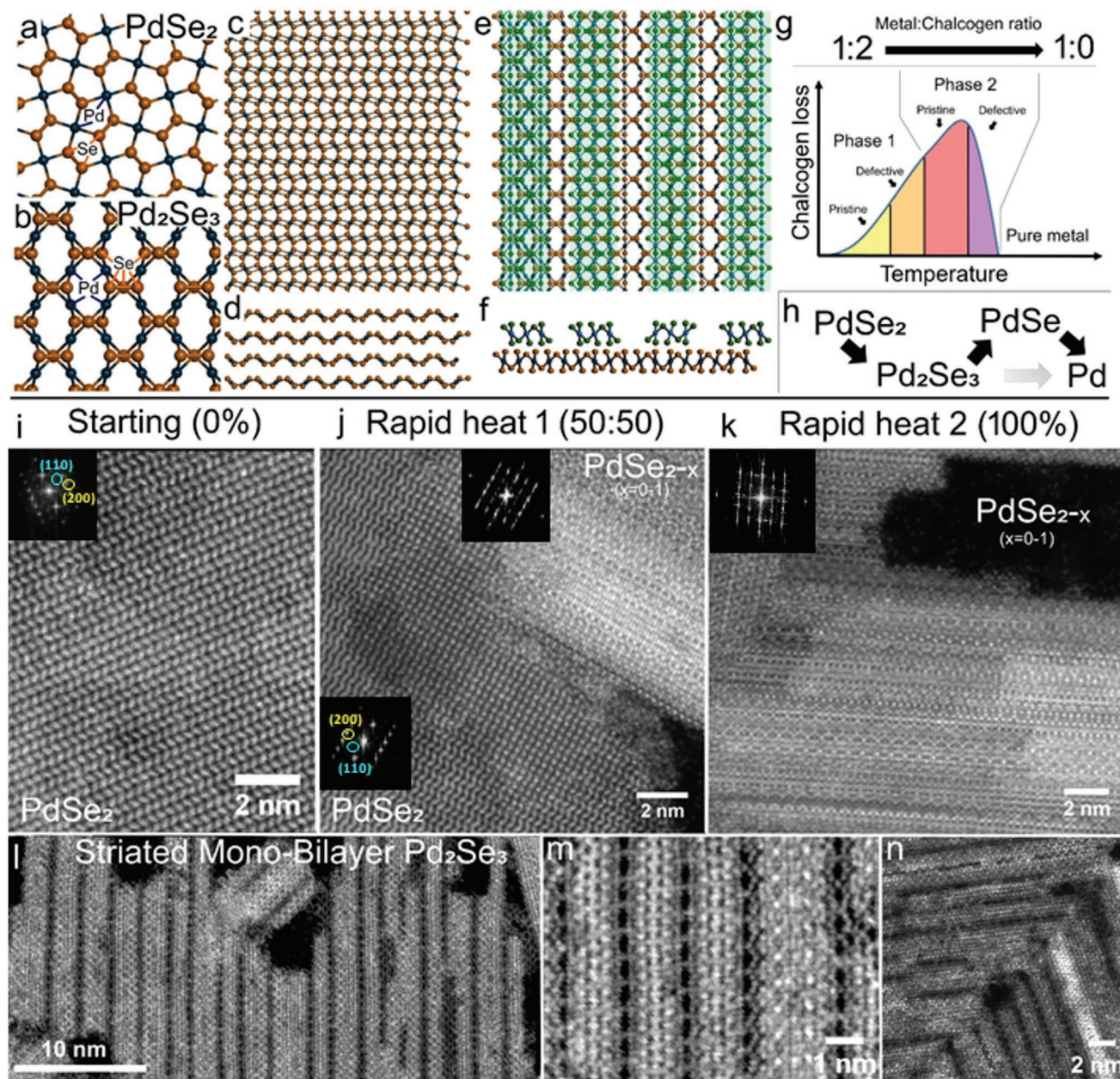


Figure 1. The phase transition from PdSe_2 to striated Pd_2Se_3 depending on temperatures. a,b) Atomic structures showing a monolayer PdSe_2 and Pd_2Se_3 , respectively. c) Extended atomic structures showing a multilayer Pd_2Se_3 with d) its side view. e) Extended atomic structures showing the striated Pd_2Se_3 with f) its side view. g) Graph showing a phase transition depending on temperature. h) Route of the phase transition. i) ADF-STEM image showing the atomic arrangement of PdSe_2 at room temperature with corresponding FFT. j) ADF-STEM image showing the interface between PdSe_2 and PdSe_{2-x} with corresponding FFTs. k) ADF-STEM image showing the PdSe_{2-x} with corresponding FFT. l) ADF-STEM image showing the monolayer Pd_2Se_3 and striated bilayer Pd_2Se_3 . m) Magnified image showing the whole striated Pd_2Se_3 . n) Grain boundary of the striated Pd_2Se_3 .

the band structure and localized states are predicted by density functional theory (DFT).

We used commercial few layered PdSe_2 (two to four layers) grown on a sapphire substrate and transferred it to an in situ heating chip for TEM studies with temperature control up to 1000 °C. When these few layered PdSe_2 films are heated in vacuum to 400–500 °C, Se loss occurs and this triggers the formation of 1D etch channels and a striated Pd_2Se_3 monolayer-bilayer 2D crystal, Figure 1c–f. According to a traditional bulk

Pd–Se phase diagram, increasing Se loss and subsequent change in metal:chalcogen ratio from 1:2 to 1:0, first leads to defective PdSe_2 (phase 1 in Figure 1g), then a phase change to a stable Se deficient form of PdSe_{2-x} ($x = 0-1$) (phase 2 in Figure 1g), and then finally to pure Pd metal. We focused on the phase change occurring from regions 1 to 2 in Figure 1g, and understanding the structural intermediates along the pathway from PdSe_2 to Pd, Figure 1h. At room temperature, the ADF-STEM images show PdSe_2 in the expected crystalline form, Figure 1i, and then

we applied a rapid heating pulse to 400 °C for 30 s to induce a partial transformation of the film, Figure 1j, where regions of PdSe_{2-x} are seen with atomically sharp interfaces to the PdSe₂ regions. A second heating pulse at 400 °C was then applied for another 30 s and caused the complete transformation into PdSe_{2-x}, Figure 1k. We repeated this experiment several times on different PdSe₂ samples to confirm the reproducibility of the results. Figure S1 in the Supporting Information shows the in situ imaging of an area of PdSe₂ transforming in real time to the PdSe_{2-x} structure. Continual heating to higher temperatures or longer duration caused excessive loss of material, further thinning and eventually the formation of pure Pd nanoparticles, Figure S2 (Supporting Information). The thinner regions of the film after transformation showed some monolayer Pd₂Se₃, and interestingly large areas of a striated Pd₂Se₃ lattice, Figure 1l,m. The striated 2D lattice consists of etched 1D channels in the bilayer Pd₂Se₃, Figure 1e,f. Grain boundaries of these 2D striated lattice sections were also observed, Figure 1n. Regions thicker than the bilayer generally exhibit complex lattice structures that we denote as PdSe_{2-x}, Figure 1k.

The 1D etched channels in Figure 1l,m are distinctly different from etching and void formation observed in other 2D crystals to date, such as hexagons in MoS₂, triangles in hBN, or circles in graphene, reflecting the differences in edge energies and stabilities for atomic loss, Figure S3 (Supporting Information). Line profile analysis confirms the monolayer-bilayer 1D channeling to form the 2D striated crystal, Figure S4 (Supporting Information). Several different types of 1D channels were observed, attributed to different amounts of local Se loss and associated defects, Figures S4–S6 (Supporting Information), one is diamond shaped (Figure S5c, Supporting Information), second is triangular shaped (Figure S5d, Supporting Information), and third is rectangular shaped (Figure S5e, Supporting Information). The triangular-shaped channel reflects the pristine underlying Pd₂Se₃ monolayer structure, as reported by previous experimental studies,^[24,29] whereas the rectangular-shaped channel has same number of Se and Pd atoms however the atoms in the hypotenuse of the triangle are aligned in a straight line. The 1D channels alternating with the periodic spacing of bilayer Pd₂Se₃ are not due to structural rearrangement but are formed by the regular expansion of void in one direction. This means that the 1D channels are influenced by 1D structural line defects.

Further atomic loss by either heating or electron beam irradiation leads to the exposure of the underlying Pd₂Se₃ monolayer, Figure 2a, indicating that the channels have a minimum width of stability. Two different types of minimum-width bilayer ribbons were observed, (Figure 2b,c), with type I being Pd₂Se₃ bilayer with AB stacking where the bottom layer is a continuous sheet and the top ribbon layer is also the Pd₂Se₃ structure, Figure 2d–i. The top ribbon section contains two ring units, indicated in Figure 2i. We did not observe any single ring unit ribbons. The type II structure, Figure 2c,j–o, contains Se vacancies in the Pd₂Se₃ (V_{Se}-Pd₂Se₃) structure and is narrower in width than the type I structure due to atomic loss and restructuring. Se vacancies occur in each bottom and top layer of the type II structure, Figure 2j–o, with 1D arrangement as shown in Figure S7 in the Supporting Information. Both type I and II structures were confirmed by comparing the

multislice ADF-STEM image simulation based on DFT relaxed atomic models. In addition, fast Fourier transforms (FFTs) of type I and II are slightly inclined than an FFT of the monolayer region, indicating that the striated structures are slightly shifted than the monolayer Pd₂Se₃.

Here, the V_{Se}-Pd₂Se₃ structures are explained by the rearrangement of atoms due to the formation of Se vacancies, even though the widths are different. Se vacancies form in the Se–Se bond rather than regions in which Se atoms bond to two Pd atoms. That is because Pd₂Se₃ possesses a lower lattice thermal conductivity due to chemical bonding of the Se–Se dumbbell than other hexagonal phases of TMDs.^[24,30] Thus, the higher the temperature of the sample, the less the thermal transport becomes, and the Se atoms in the Se–Se bond are preferentially removed. The other Se atoms rearrange, as shown in Figure S7c in the Supporting Information, to maintain the bonding saturation of Pd atoms. Dynamic changes are often seen between different ribbon structures, Figure S8 (Supporting Information). Larger width ribbons in the striated Pd₂Se₃ structures are made up of the two building blocks from Figure 2, shown in Figure 3. The top region is V_{Se}-Pd₂Se₃ and the bottom region is the pristine structure. The rearrangements of atoms are the same as the atomic behavior depicted in Figure 2n,o, and this structure has long length.

The channeling can start even in the three-layer systems, Figure 4a, which shows the boundaries of the mono-, bi-, and trilayer regions. The striated Pd₂Se₃ with 1D channels is clear in the bilayer region. In the trilayer region, distinct 1D channels are not clear as in the bilayer region, but partial etching is seen in the yellow-green circles. Further heating and material loss eventually lead to the formation of interconnecting 1D nanowires made up of the bilayer nanoribbons between regions of the 2D striated lattice, Figure 4. The nanowires in Figure 4 are being supported by the underlying thin amorphous carbon layer. Figure 4c shows a near atomically sharp point contact at the mid-point of the nanowire.

The unique 1D channels in the striated 2D lattice may provide avenues to tune the optoelectronic properties of Pd₂Se₃. We computationally assessed different stacking structures with/without defects (Figure 5 and Figure S11, Supporting Information) based on DFT (see the Experimental Section). In Figure 5a–j and Figure S11a–e in the Supporting Information, the top layer varies from partially covered by single and double pristine ribbons to fully covered (i.e., bilayer Pd₂Se₃) with AB stacking order. The partial stacking structure with single ribbons exhibits a band gap around 0.3 eV (Figure 5a), which is between >0.5 eV for single pristine layer^[30] and 0 eV for the metallic full AB stacking structure (Figure S11a, Supporting Information). Therefore, the coverage or channel width of the stacking layer could be an effective factor to tune the band gap. Moreover, the dispersion becomes less dispersive, suggesting an enhanced band effective mass and therefore reduced carrier mobility. From the projected density of states (Figure 5b,c), it could be seen that Pd 4d are dominant orbitals, similar to the monolayer. The intra-mixing of Pd 4d orbitals and overlap between Se 4p orbitals are shown to determine the electronic properties of monolayer Pd₂Se₃.^[30] In our case, the stacking layer plays a more interesting role. As shown in Figure 5d,e, while states close to the conduction band minimum (CBM)

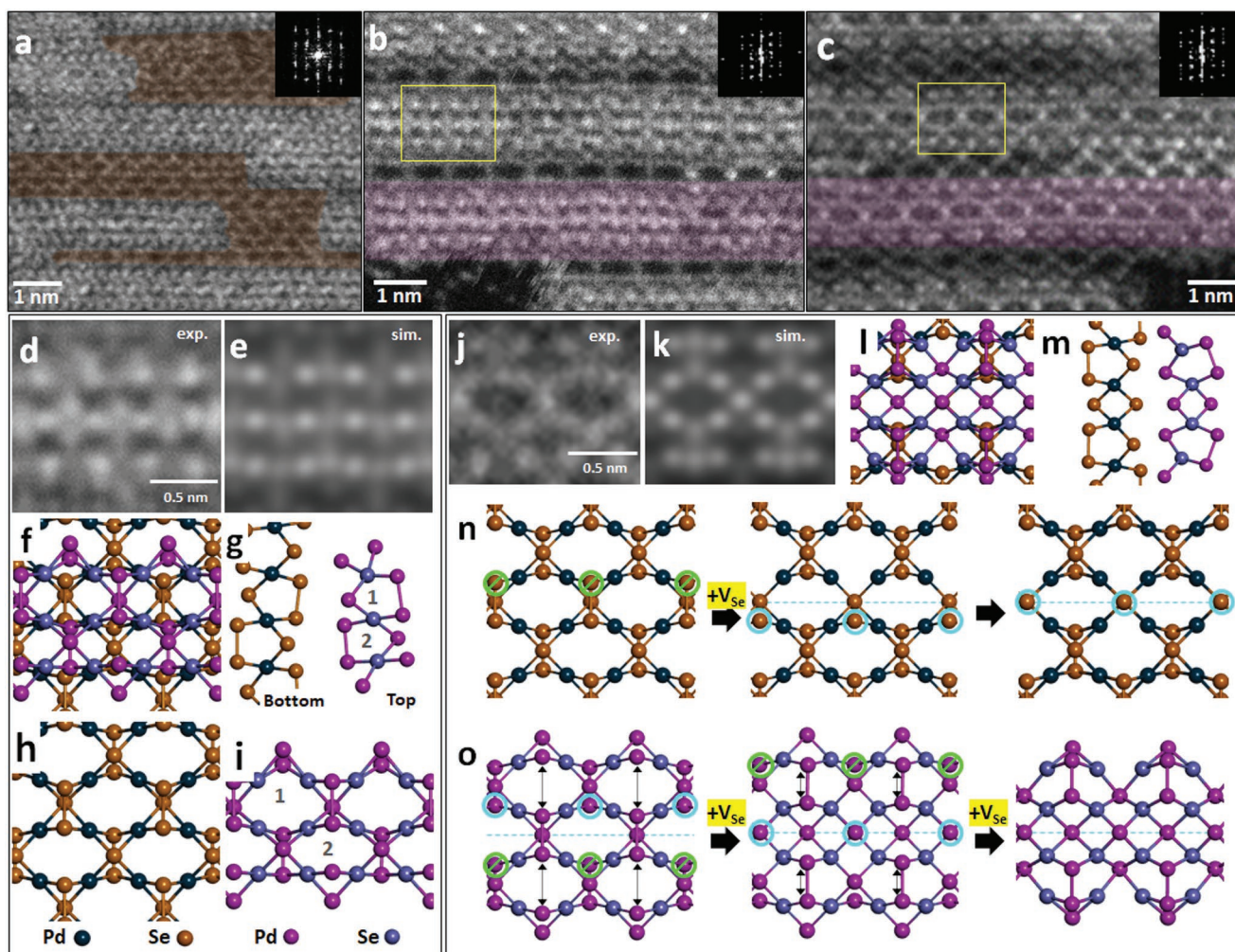


Figure 2. Basic structures of the striated Pd_2Se_3 with the thinnest width. a) ADF-STEM image showing the monolayer (shading orange regions) and bilayer Pd_2Se_3 with corresponding FFT. b,c) ADF-STEM images showing AB stacked Pd_2Se_3 and $\text{V}_{\text{Se}}\text{-Pd}_2\text{Se}_3$, respectively, with each corresponding FFT. d) Magnified image of the yellow box in (b), which indicates the AB stacked bilayer Pd_2Se_3 . e) Multislice ADF-STEM image simulation corresponding to f) the relaxed atomic model with g) the side view. h,i) Atomic models of the top and bottom layers, respectively. j) Magnified image of the yellow box in (c), which indicates the bilayer Pd_2Se_3 band involving Se vacancies. k) Multislice ADF-STEM image simulation corresponding to l) the relaxed atomic model. g) Side view of (l). n,o) Sequential atomic models represent the process of atom rearrangement on the structure.

exhibit delocalized character, the states near valence band maximum (VBM) are heavily localized on the stacking layer, which suggests the determining effects of stacking modulation. For instance, as shown in our experiments, once the in-plane channel width between stacking layers is reduced, extra states emerge in the band gap (Figure 5f). These states are hybridized from Pd 4d orbitals and Se 4p orbitals (Figure 5g,h) and mostly localized on the stacking layers (Figure 5i,j).

On the other hand, the band structure and density of states for defected structures (Figure 5k–o) suggest a semiconductor-metal transition induced by the structural disorder in the top layer. The band gap shown for the pristine structure in Figure 5a could be completely filled by the Pd 4d orbitals and Se 4p hybrid orbitals by introducing one-row defects in the stacking layer (Figure 5k). The states 0.15 eV below and above the Fermi level are shown in Figure 5n,o and compared to Figure 5d,e for the ordered structure. Due to the presence of defects, these frontier states are localized close to the

interface, yet mostly on the stacking layer. In contrast, these frontier states and thus band gap are insensitive to the similar defects in the substrate layer (Figure S11f–j, Supporting Information). The effects of stacking-layer thickness and more detailed quantification of defect effects would be interesting for future study.

These results show that unique nanoscale anisotropic 2D crystal structures can be created using large-scale transformation of existing layered materials. The striated structures are not observed in hexagonal phase TMDs, such as MoS_2 and WS_2 , and suggest that penta- PdSe_2 might offer advantages in the area of the thermal phase transition in 2D materials. Through the calculated electronic structures, their unique striated stacking layer can suggest the semiconductor-metal transition. This shows that understanding the pathways for reconstruction is important and future work will explore methods for a generalized framework for a new family of ultrathin films from phase transformation of layered systems with binary elements.

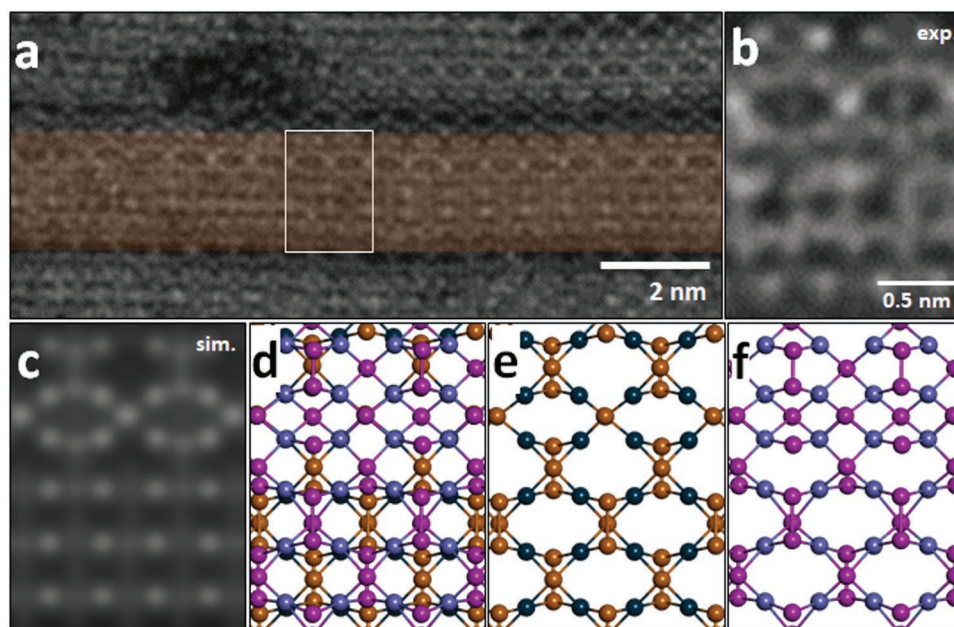


Figure 3. a) ADF-STEM image showing the combined structure of the pristine AB structure and the Se vacancies-involved structure. b, c) ADF-STEM images and multislice ADF-STEM image simulation corresponding to the atomic model showing combined structures between the pristine structure and the V_{Se} -Pd $_2$ Se $_3$ structure. d) Atomic model of the combined structure. e, f) The detailed atomic models of the top and bottom layers, respectively.

Experimental Section

Multilayer PdSe $_2$ and Transfer: The PdSe $_2$ was bought, which was synthesized using chemical vapor deposition on c-cut sapphire through 2D semiconductors. Transfer was achieved by spin-coating the sample with a supporting poly(methyl acrylate) (PMMA) scaffold (8 wt%, $M_w = 495k$). The PMMA/PdSe $_2$ stack was separated from sapphire substrate by KOH etching (1 M) at 60 °C. The PMMA/PdSe $_2$ film was transferred via clean

glass slides to deionized water to rinse residue from the PdSe $_2$ side, which was repeated several times. The film was then transferred to the sample chip, allowed to dry overnight, and then heated on a hot plate at 150 °C to drive off remaining water and promote sample adhesion.

TEM with an In Situ Heating Holder: ADF-STEM was conducted using an aberration-corrected JEOL ARM200 STEM equipped with a JEOL corrector operated at an accelerating voltage of 80 kV located at the David Cockayne Center. Dwell times of 5–20 μ s and a pixel size of 0.006 nm px $^{-1}$ were used

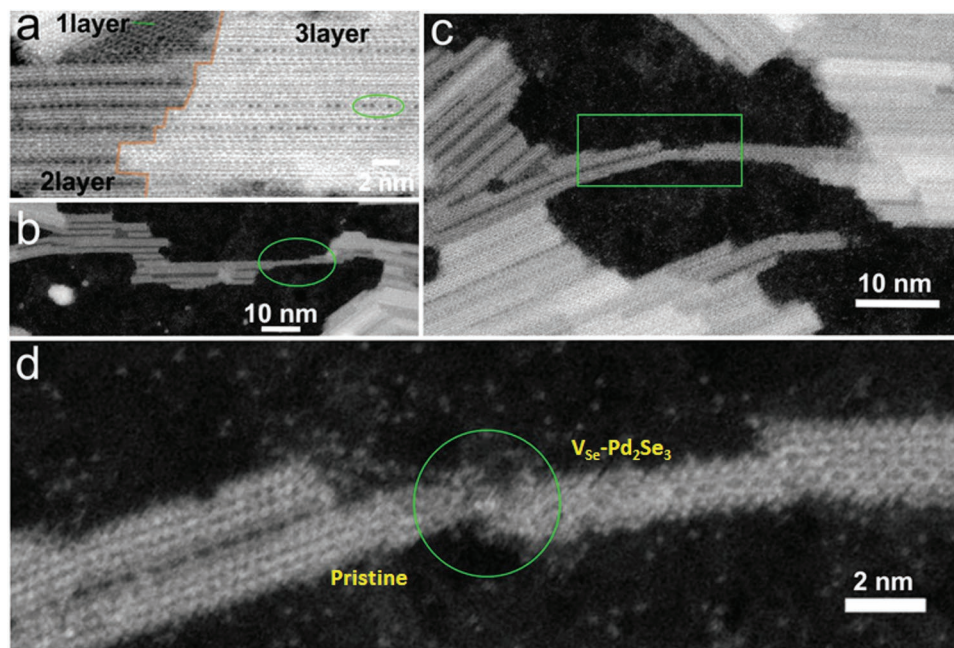


Figure 4. Narrowing to single wire between the pristine and V_{Se} -Pd $_2$ Se $_3$. a) Whole regions showing from the monolayer to trilayer and each interface. b) Single wire forming from the Pd $_2$ Se $_3$. c) Single nanowire before breaking. d) Magnified image of (c) showing the detail structures of broken junction of the wire containing both structures.

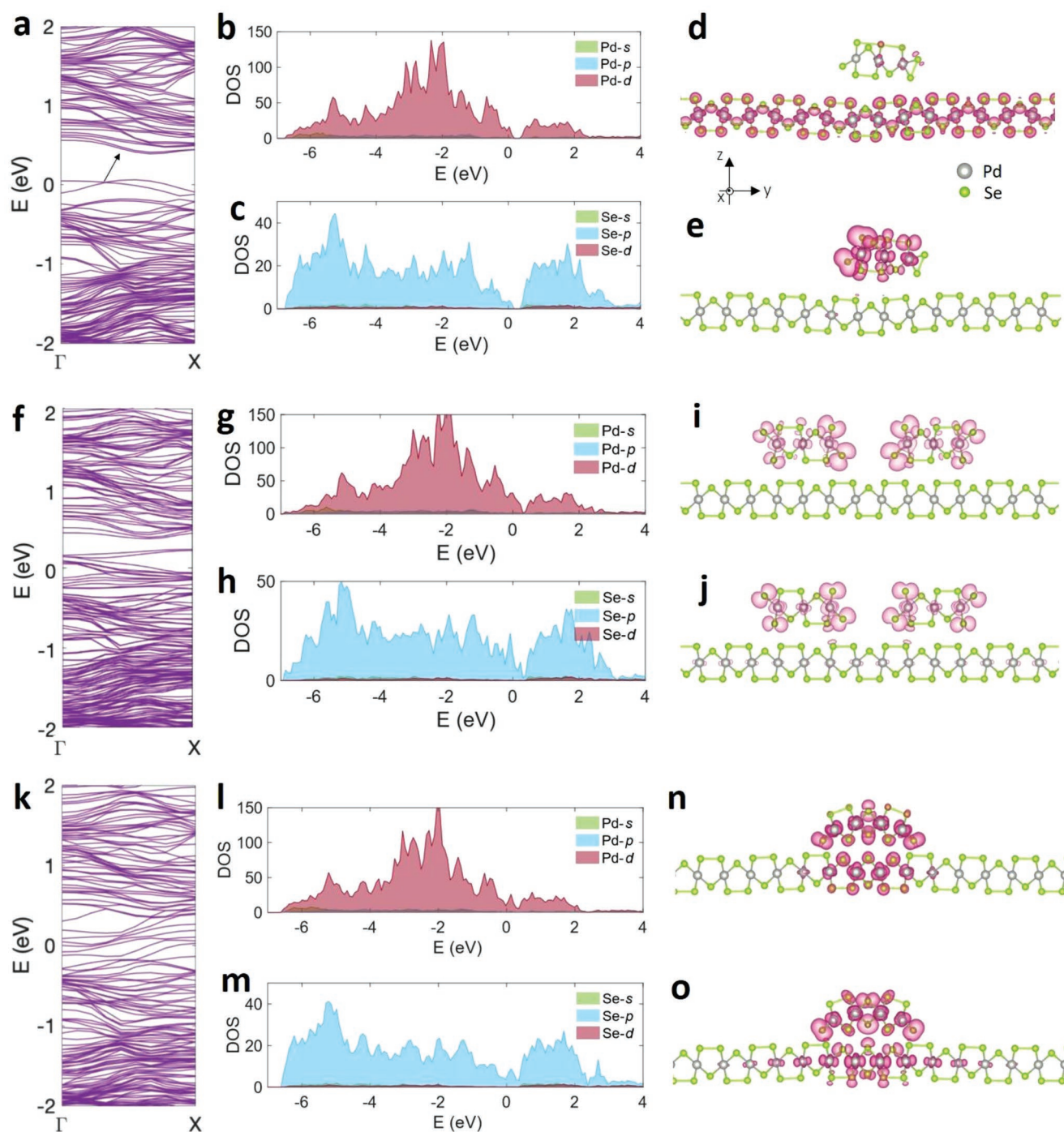


Figure 5. Electronic properties calculated from DFT for ordered and defected stacking layer. a) Band structure showing an indirect band gap (≈ 0.3 eV) is observed for the ordered structure. b,c) Density of states of the ordered structure. d,e) CFBM and VBM of the ordered structure, respectively. f) Band structure showing no band gap when two channels exist as top layers. g,h) Density of states of the ordered structure with two channels. i,j) Frontier states within 0.15 eV above/below Fermi level for the ordered structure having two channels. k) Total band structure of the disordered structure. l,m) Density of states for the disordered structure, in which a row of Se atoms is missing in the stacking layer. n,o) States within 0.15 eV above/below Fermi level for the disordered structure.

for imaging with a convergence semi-angle of 31.5 mrad, a beam current of 44 pA, and inner–outer acquisition angles of 49.5–198 mrad.

Temperature-dependent ADF-STEM imaging up to 400 °C was performed using a commercially available in situ heating holder from DENS Solutions (SH30-4M-FS). Focused ion beam (FIB) was used

to cut open slits in the Si_3N_4 membrane to enable suspended PdSe_2 samples for imaging. Heating the sample was achieved by passing a current through a platinum resistive coil embedded in the TEM chip (DENS Solutions DENS-C-30). The resistance of the platinum coil was monitored in a four-point configuration, and the temperature was

calculated using the Callendar–Van Dusen equation (with calibration constants provided by the manufacturer). Slits were fabricated in the Si₃N₄ membranes using FIB milling before transferring the PdSe₂.

Image Processing and Simulation: ImageJ was used to process the ADF images. Multislice image simulations for ADF images were performed using the multislice method implemented in the JEMS software. Parameters for image simulations were based on the experimental condition of the JEOL ARM200. The chromatic aberration at 80 kV was 1 mm with an energy spread of 0.60 eV. The probe size was 65 pm and the convergence semi-angle was 31.5 mrad. The angle range for dark field imaging was from 49.5 to 198 mrad. Spherical aberration was 5 μm.

DFT and Electronic Calculations: In order to study the structural and electrical properties of the synthesized striated Pd₂Se₃, first-principles calculations were used based on the DFT implemented in the Vienna Ab initio Simulation Package.^[31,32] All the DFT relaxations were performed using an 8 × 1 × 1 supercell (lower continuous layer) in two consequential steps: i) initial relaxation within the generalized gradient approximation with Perdew–Burke–Ernzerhof augmented by DFT-D3 method with Becke–Johnson damping for the interlayer dispersive interaction.^[33,34] The initial relaxation is then followed by ii) meta-generalized-gradient approximation with strongly constrained and appropriately normed (SCAN), plus the nonlocal correlation part from the rVV10 vdW density functional for the van der Waals interactions.^[35,36] Projector-augmented wave potentials were employed with 500 eV energy cutoff. The 10 (4s¹4d⁹) valence electrons for Pd and 6 (4s²4p⁴) for Se were treated explicitly. The first Brillouin zone was sampled by the tetrahedron method on a 12 × 1 × 1 k-mesh. All structures were relaxed until the force on each atom was less than 0.01 meV Å⁻¹. To further confirm the dynamical stability of the relaxed structure, Born–Oppenheimer molecular dynamics were carried out. The 8 × 1 × 1 supercell was equilibrated in a Nose–Hoover NVT thermostat at 300 K for about 10 ps with a time step of 1 fs. Here, SCAN+rVV10 was used. It was noted from these MD simulations that the relaxed striated structures were dynamically stable at room temperature. Since the inclusion of spin-orbital coupling (SOC) was found to change the dispersion negligibly,^[31] no SOC was included in all the calculations.

Supporting Information

Supporting Information is available from the Wiley Online Library or from the author.

Acknowledgements

J.H.W. thanks the support from the Royal Society and the ERC Consolidator grant (725258 CoG 2016 LATO). The authors thank Diamond Light Source for access and support in use of the electron Physical Science Imaging Centre (EM16854) that contributed to the results presented here.

Conflict of Interest

The authors declare no conflict of interest.

Keywords

1D channels, 2D crystals, Pd₂Se₃, PdSe₂, Se vacancies, STEM

Received: July 4, 2019

Revised: August 21, 2019

Published online: September 27, 2019

- [1] P. L. Harrison, R. A. Farrar, *J. Mater. Sci.* **1981**, 16, 2218.
- [2] S. E. Offerman, N. H. Dijk, J. Sietsma, S. Grigull, E. M. Lauridsen, L. Margulies, H. F. Poulsen, M. Th. Rekveldt, S. van der Zwaag, *Science* **2002**, 298, 1003.
- [3] M. I. McMahon, R. J. Nemes, *Chem. Soc. Rev.* **2006**, 35, 943.
- [4] D. A. Porter, K. E. Easterling, M. Y. Sherif, *Phase Transformations in Metals and Alloys*, CRC Press, Boca Raton, FL **2009**.
- [5] G. Patriarche, F. Glas, M. Tchernycheva, C. Sartet, L. Largeau, J.-C. Harmand, G. E. Cirlin, *Nano Lett.* **2008**, 8, 1638.
- [6] K. J. Reeson, J. Stoemenos, P. L. F. Hemment, *Thin Solid Films* **1990**, 191, 147.
- [7] A. Polman, P. A. Stolk, D. J. W. Mous, W. C. Sinke, *J. Appl. Phys.* **1990**, 67, 4024.
- [8] G. H. Ryu, A. France-Lanord, Y. Wen, S. Zhou, J. C. Grossman, J. H. Warner, *ACS Nano* **2018**, 12, 11638.
- [9] Q. Chen, H. Li, S. Zhou, W. Xu, J. Chen, H. Sawada, C. S. Allen, A. I. Kirkland, J. C. Grossman, J. H. Warner, *ACS Nano* **2018**, 12, 7721.
- [10] S. Wang, H. Li, H. Sawada, C. S. Allen, A. I. Kirkland, J. C. Grossman, J. H. Warner, *Nanoscale* **2017**, 9, 6417.
- [11] K. Liu, M. Lihter, A. Sarathy, S. Caneva, H. Qiu, D. Deiana, V. Tileli, D. T. Alexander, S. Hofmann, D. Dumcenco, *Nano Lett.* **2017**, 17, 4223.
- [12] H.-P. Komsa, S. Kurasch, O. Lehtinen, U. Kaiser, A. V. Krashenninnikov, *Phys. Rev. B* **2013**, 88, 035301.
- [13] S. Wang, G.-D. Lee, S. Lee, E. Yoon, J. H. Warner, *ACS Nano* **2016**, 10, 5419.
- [14] G. H. Ryu, J. Lee, N. Y. Kim, Y. Lee, Y. Kim, M. J. Kim, C. Lee, Z. Lee, *2D Mater.* **2016**, 3, 014002.
- [15] G. H. Ryu, H. J. Park, J. Ryou, J. Park, J. Lee, G. Kim, H. S. Shin, C. W. Bielawski, R. S. Ruoff, S. Hong, Z. Lee, *Nanoscale* **2015**, 7, 10600.
- [16] D. Voiry, A. Mohite, M. Chhowalla, *Chem. Soc. Rev.* **2015**, 44, 2702.
- [17] K.-A. N. Duerloo, Y. Li, E. J. Reed, *Nat. Commun.* **2014**, 5, 4214.
- [18] H. Zhang, L.-M. Liu, W.-M. Lau, *J. Mater. Chem. A* **2013**, 1, 10821.
- [19] Y. Li, K.-A. N. Duerloo, K. Wauson, E. J. Reed, *Nat. Commun.* **2016**, 7, 10671.
- [20] Y. Wang, J. Xiao, H. Zhu, Y. Li, Y. Alsaid, K. Y. Fong, Y. Zhou, S. Wang, W. Shi, Y. Wang, A. Zettl, E. J. Reed, X. Zhang, *Nature* **2017**, 550, 487.
- [21] J. Sun, H. Shi, T. Siegrist, D. J. Singh, *Appl. Phys. Lett.* **2015**, 107, 153902.
- [22] L. X. Benedict, N. G. Chopra, M. L. Cohen, A. Zettl, S. G. Louie, V. H. Crespi, *Chem. Phys. Lett.* **1998**, 286, 490.
- [23] Y. Wang, Y. Li, Z. Chen, *J. Mater. Chem. C* **2015**, 3, 9603.
- [24] J. Lin, S. Zuluaga, P. Yu, Z. Liu, S. T. Pantelides, K. Suenaga, *Phys. Rev. Lett.* **2017**, 119, 016101.
- [25] A. D. Oyedele, S. Yang, L. Liang, A. A. Puzetzy, K. Wang, J. Zhang, P. Yu, P. R. Pudasaini, A. W. Ghosh, Z. Liu, C. M. Rouleau, B. G. Sumpter, M. F. Chisholm, W. Zhou, P. D. Rack, D. B. Geohegan, K. Xiao, *J. Am. Chem. Soc.* **2017**, 139, 14090.
- [26] F. Gronvold, E. Rost, *Acta Crystallogr.* **1957**, 10, 329.
- [27] J. Chen, G. H. Ryu, S. Sinha, J. H. Warner, *ACS Nano* **2019**, 13, 8256.
- [28] A. D. Oyedele, S. Yang, T. Feng, A. V. Haglund, Y. Gu, A. A. Puzetzy, D. Briggs, C. M. Rouleau, M. F. Chisholm, R. R. Unocic, D. Mandrus, H. M. Meyerlll, S. T. Pantelides, D. B. Geohegan, K. Xiao, *J. Am. Chem. Soc.* **2019**, 141, 8928.
- [29] S. Zuluaga, J. Lin, K. Suenaga, S. T. Pantelides, *2D Mater.* **2018**, 5, 035025.
- [30] S. S. Naghavi, J. He, Y. Xia, C. Wolverton, *Chem. Mater.* **2018**, 30, 5639.
- [31] G. Kresse, J. Furthmüller, *Phys. Rev. B* **1996**, 54, 11169.
- [32] G. Kresse, J. Furthmüller, *Comput. Mater. Sci.* **1996**, 6, 15.
- [33] J. Sun, A. Ruzsinszky, J. P. Perdew, *Phys. Rev. Lett.* **2015**, 115, 036402.
- [34] J. Sun, R. C. Remsing, Y. Zhang, Z. Sun, A. Ruzsinszky, H. Peng, Z. Yang, A. Paul, U. Waghmare, X. Wu, M. K. Klein, J. P. Perdew, *Nat. Chem.* **2016**, 8, 831.
- [35] P. E. Blöchl, *Phys. Rev. B* **1994**, 50, 17953.
- [36] G. Kresse, D. Joubert, *Phys. Rev. B* **1999**, 59, 1758.